

Climate Dynamics

Intraseasonal Variability in South America during the Cold Season

--Manuscript Draft--

Manuscript Number:	
Full Title:	Intraseasonal Variability in South America during the Cold Season
Article Type:	Original Article
Keywords:	Intraseasonal Variability; winter; Outgoing Longwave Radiation; South America.
Corresponding Author:	Mariano Sebastián Alvarez, Lic. Centro de Investigaciones del Mar y la Atmósfera, CONICET-UBA, DCAO/FCEN, UMI IFAEI/CNRS Buenos Aires, Buenos Aires ARGENTINA
Corresponding Author Secondary Information:	
Corresponding Author's Institution:	Centro de Investigaciones del Mar y la Atmósfera, CONICET-UBA, DCAO/FCEN, UMI IFAEI/CNRS
Corresponding Author's Secondary Institution:	
First Author:	Mariano Sebastián Alvarez, Lic.
First Author Secondary Information:	
Order of Authors:	Mariano Sebastián Alvarez, Lic. Carolina Susana Vera, Dr George N. Kiladis, Dr Brant Liebmann, Dr
Order of Authors Secondary Information:	
Abstract:	<p>Intraseasonal (IS) variability in South America is analyzed during the cold season using 10-90 day bandpass filtered OLR anomalies (FOLR). IS variability explains a large percentage of variance and exhibits maximum values over Paraguay, northeastern Argentina, and southern Brazil. The leading pattern of FOLR, as isolated from an EOF analysis, (Cold Season IS pattern, CSIS), is characterized by a monopole centered over southeastern South America (SESA) with a northwest-southeast orientation. CSIS activity induces a large modulation on daily precipitation anomalies, especially on both wet spells and daily precipitation extremes, which are favored during positive (wet) CSIS phases.</p> <p>Large-scale OLR anomalies over the tropical Indian and west Pacific Oceans associated with CSIS are similar to those linked to MJO. In addition, large-scale circulation anomalies in the Southern Hemisphere exhibit evidence of Southern Annular Mode (SAM) activity as well as of Rossby wave-like patterns. Positive precipitation anomalies in SESA are favored during wet CSIS phases by the intensification of a cyclonic anomaly located further south, which is discernible over the southeastern Pacific for at least 14 days before CSIS peaks. The cyclonic anomaly evolution is accompanied by the intensification of an upstream anticyclonic anomaly, which remains stationary in the southeastern Pacific during the days before the CSIS peak and then extends poleward over the Antarctica Peninsula. We speculate that the stationary behavior of the anticyclonic center is favored by a hemispheric circulation anomaly pattern resembling that associated with a negative SAM phase and a favored wavenumber 3-4 pattern at middle latitudes.</p>
Suggested Reviewers:	<p>Leila Carvalho UC Santa Barbara, USA leila@eri.ucsb.edu</p> <p>Tercio Ambrizzi University of Sao Paulo, Brazil</p>

	ambrizzi@model.iag.usp.br
	Iracema Cavalcanti INPE, Brazil iracema.cavalcanti@cpfec.inpe.br
	Rene Garreaud University of Chile, Chile rgarreau@dgf.uchile.cl
	Kingtse Mo NOAA/NCEP/CPC Kingtse.Mo@noaa.gov

Intraseasonal Variability in South America during the Cold Season

Mariano S. Alvarez¹, C. S. Vera¹, G. N. Kiladis², B. Liebmann²

¹Centro de Investigaciones del Mar y la Atmósfera, CONICET-UBA, DCAO/FCEN, UMI IFAECI/CNRS.
Buenos Aires, Argentina

²Earth System Research Laboratory/NOAA, CIRES/University of Colorado, Boulder, Colorado, USA

Corresponding author address: Mariano S. Alvarez, CIMA, Ciudad Universitaria, Pabellón II-2do. Piso (C1428EGA), Buenos Aires, Argentina.
E-mail: alvarez@cima.fcen.uba.ar

Abstract

Intraseasonal (IS) variability in South America is analyzed during the cold season using 10-90 day bandpass filtered OLR anomalies (FOLR). IS variability explains a large percentage of variance and exhibits maximum values over Paraguay, northeastern Argentina, and southern Brazil. The leading pattern of FOLR, as isolated from an EOF analysis, (Cold Season IS pattern, CSIS), is characterized by a monopole centered over southeastern South America (SESA) with a northwest-southeast orientation. CSIS activity induces a large modulation on daily precipitation anomalies, especially on both wet spells and daily precipitation extremes, which are favored during positive (wet) CSIS phases.

Large-scale OLR anomalies over the tropical Indian and west Pacific Oceans associated with CSIS are similar to those linked to MJO. In addition, large-scale circulation anomalies in the Southern Hemisphere exhibit evidence of Southern Annular Mode (SAM) activity as well as of Rossby wave-like patterns. Positive precipitation anomalies in SESA are favored during wet CSIS phases by the intensification of a cyclonic anomaly located further south, which is discernible over the southeastern Pacific for at least 14 days before CSIS peaks. The cyclonic anomaly evolution is accompanied by the intensification of an upstream anticyclonic anomaly, which remains stationary in the southeastern Pacific during the days before the CSIS peak and then extends poleward over the Antarctica Peninsula. We speculate that the stationary behavior of the anticyclonic center is favored by a hemispheric circulation anomaly pattern resembling that associated with a negative SAM phase and a favored wavenumber 3-4 pattern at middle latitudes.

Keywords: Intraseasonal Variability, winter, Outgoing Longwave Radiation, South America.

33 Introduction

34 Intraseasonal (IS) variability in the South American summer has been thoroughly studied (e.g.,
35 Nogués-Paegle and Mo 1997; Liebmann et al. 1999), and is usually described through the activity of the
36 leading Empirical Orthogonal Function (EOF) pattern of convection or precipitation IS variability. Typically,
37 IS variability is defined to include periods from 10 to 90 days. The pattern exhibits centers of action of
38 opposite sign in the South Atlantic Convergence Zone (SACZ) and in the subtropical region of southeastern
39 South America (SESA), respectively. Its variability strongly influences the occurrence and intensity of
40 extreme events of both daily precipitation (e.g., Liebmann et al. 2004) and daily surface temperature (e.g.,
41 Cerne and Vera 2011). Little attention has been devoted to wintertime IS variability, however, despite high-
42 impact phenomena that affect subtropical and extra-tropical South America, such as blocking and cut-off
43 lows, which exhibit periods longer than those typically associated with synoptic scales.

44 There is much evidence of the relevance of circulation variability on IS timescales in the Southern
45 Hemisphere (SH). Dynamics associated with IS variability in the SH circulation seems to be more complex
46 and dominated by shorter wave numbers than in the Northern Hemisphere (Ghil and Mo 1991). Kidson
47 (1999) explored IS variability of the 300-hPa streamfunction daily anomalies using EOF analysis. The
48 resulting leading patterns display oscillatory features on IS time scales exhibiting wavenumbers 4-5, which
49 propagate eastward and are mainly confined to middle and high latitudes. In addition, through both
50 observational analyses and numerical simulations, it has been shown that IS oscillations in the SH winter are
51 associated with wavetrains extending over the Indian-South Pacific sector that split near Australia, giving rise
52 downstream to two wavetrains, one along subpolar and the other along subtropical latitudes (Berbery et al.
53 1992; Ambrizzi et al. 1995). Moreover, the subpolar and tropical wavetrains merge over central or eastern
54 South Pacific and penetrate equatorward into South America. Mo and Higgins (1998) thoroughly analyzed IS
55 circulation variability in the South Pacific region during austral winter and found that the first two modes
56 resemble those named the “Pacific-South American” (PSA, Mo and Ghil 1987) pattern associated with
57 Rossby wavetrains extending from the central and western tropical Pacific region and arcing northeastward,
58 towards South America. Moreover, Mo and Higgins (1998) found that the two PSA patterns (PSA1 and
59 PSA2) are in quadrature with each other and are dominated by wavenumber 3 in midlatitudes. Robertson and

Mechoso (2003) pointed out that geographically fixed circulation regimes with variability on IS time scales and spatial structures similar to the PSA are more pronounced during the cold season. On the other hand, the tropical influence on the extratropical IS variability of the SH seems to be less intense in winter than summer (Berbery and Nogués-Paegle 1993), suggesting that internal variability within the storm tracks might dominate during winter.

IS variability over Antarctica and the Southern oceans has also been documented. The Southern Annular Mode (SAM), a pattern that displays negative (positive) geopotential heights anomalies over Antarctica and positive (negative) anomalies at middle latitudes in association with a wavenumber 3-4 pattern during its positive (negative) phase, seems to be primarily responsible for that variability (e.g., Baba et al. 2006; Yu et al. 2011 and references therein). In agreement, Kidson (1999) shows that the SAM, known for its large interannual variability, also exhibits considerable activity on IS time scales. In addition, the influence of the activity of eastward propagating waves over the western South Pacific, partially associated with variability in the tropics, has also been identified as relevant to the IS variability of western Antarctica (e.g., Yu et al. 2011).

In this study we document the principal characteristics of IS variability in South America during the cold season and relate it to that observed in both the SH circulation and tropical convection. We base our study on the analysis of the activity of the leading pattern of 10-90 day bandpass filtered OLR anomalies in South America. We selected OLR to describe the IS variability instead of precipitation because it is a continuous variable with no extended gaps of missing data, as those exhibited by the daily precipitation records in South America. Previous work (e.g., Gonzalez et al. 2008) has shown that the OLR anomalies are able to represent the main features of South American IS variability.

The paper is organized as follows: datasets and methodology are described in Section 2. Section 3 describes the basic climatology of cold season IS variability and the main characteristics of the leading EOF pattern of filtered OLR anomalies. Regression maps are also presented to analyze the relationship between the pattern activity and circulation anomalies in South America and in the SH. A discussion of the relevance of the leading EOF pattern in describing precipitation variability with a focus on its role in modulating the

frequency of regional wet spells and extreme rain events is also presented. Section 4 includes a summary and conclusions.

Data and Methodology

Data

The study encompasses the data analysis from 28 austral cold seasons between 1979 and 2006. The cold season is defined as the 151-day period centered in the June-July-August (JJA) trimester. OLR data were obtained from the National Oceanic and Atmospheric Administration (NOAA) gridded dataset (Liebmann and Smith 1996). Daily means for geopotential heights, winds and vertical velocity omega from the National Centers for Environmental Prediction-National Center for Atmospheric Research (NCEP-NCAR) reanalysis dataset (Kalnay et al. 1996) were also used. All datasets are displayed on a 2.5° latitude x 2.5° longitude grid. Daily precipitation station data were retrieved from CLARIS-LPB online database available at <http://wp32.at.fcen.uba.ar/>. Daily precipitation on a 2.5 degree grid developed by Liebmann and Allured (2005) were also used and will be hereafter referred as LA05 database.

Methodology

The seasonal cycle was constructed by smoothing the climatological daily means with a 31-point moving average. Daily anomalies were then calculated at every grid point by subtracting the seasonal cycle. Filtered OLR anomalies (FOLR) were obtained from daily anomalies band-passed using a 10-90-day bandpass Lanczos filter with 101 weights (Duchon 1979).

EOF analysis based on the covariance matrix was applied to FOLR to isolate the dominant pattern of the OLR variability on IS timescales. The leading pattern is hereafter named Cold Season IS (CSIS) and the associated principal component was standardized and called the CSIS index. Positive (negative) values of the CSIS index will be referred to as the wet (dry) phase of the leading pattern.

Lagged linear regression maps of anomalies of OLR, daily precipitation and both geopotential heights and winds at 250 hPa, were calculated against the CSIS index to describe the main features of the circulation anomalies associated with CSIS evolution in the SH and in particular in South America. Regressions were scaled to a value of one standard deviation of the CSIS index and one day lagged increments were considered. The correlation coefficient enables the statistical significance of the local linear relationship between CSIS and the dependent variable at any given grid point to be assessed. The regressed values are only displayed if they are significant at the 95% level.

The influence of CSIS activity on daily precipitation in SESA was further studied. Special attention was paid to exploring two specific issues related to CSIS activity: whether it affects the persistence of daily precipitation occurrence (wet spells) and whether it influences the occurrence of daily precipitation extremes. The daily precipitation variability in SESA was described using the information provided by nine precipitation stations retrieved from the CLARIS-LPB database (Table 1). The spatial mean of the daily precipitation time series from those stations was computed, and the resulting series is called the SESA precipitation time series.

Tolika and Maheras (2005) defined a wet spell as a period of consecutive days with rainfall above a particular threshold (e.g., 1 mm) in order to exclude light precipitation and to account for the limited accuracy of rain gauges (Zolina et al. 2005). In addition, the CCL/CLIVAR Working Group on Climate Change Detection defined as moderate wet days those with precipitation above the 75th percentile of the distribution of daily precipitation amounts of at least 1 mm (Peterson et al. 2001). Therefore, in this study we define wet spells as those periods of at least two consecutive days with rainfall above 1 mm. In a similar way, P75 wet spells were defined as those periods of at least two consecutive days with rainfall above the 75th percentile of daily significant precipitation (17.9 mm for SESA precipitation time series). Also, hereafter P75 wet days refer to those individual days in which precipitation was larger than the 75th percentile value. Daily extreme precipitation events in SESA were defined as those days in which precipitation was greater than the 90 and 99 percentiles of the wet days (30.9 and 65.9 mm) identified from SESA daily precipitation time series.

Composite maps of geopotential height anomalies at 250 hPa based on periods associated with wet spells and CSIS activity were also made to better understand the CSIS influence in modulating the circulation

anomalies favorable to wet-spell occurrence in SESA. Composite maps were tested using a student's *t*-test with a 95% confidence level.

Results

Climatology of IS variability

The standard deviation of FOLR was computed to estimate the IS mean variability during the cold season. Figure 1a shows that the region of maximum standard deviation is located over SESA, elongated along a northwest-southeast (NW-SE) axis. During the cold season, IS variability explains between 30% and 40% of the total variance (not shown) over SESA. For comparison purposes, the corresponding FOLR standard deviation for the warm season (defined following Gonzalez et al. 2008, as the 151 day-period centered in December-January-February) is also included (Figure 1b). It is known that IS mean variability during the warm season, as described in previous studies (e.g., Liebmann et al. 1999), exhibits the largest amplitudes over the SACZ region. A comparison between panels of Figure 1 shows that the maximum of IS variability associated with the SACZ during the warm season is not present during the cold season, as the SACZ primarily is a warm season feature. Furthermore, during the cold season IS variability over SESA is lower amplitude and displaced southward compared to the warm season.

The power spectrum of the FOLR time series located at 55°W, 25°S, which is the region of maximum variance explained by the IS variability (not shown), displays peaks at around 42-51 days, 23-30 days and around 15-17 days, but none are statistically significant. In agreement, Mo and Higgins (1998) and Robertson and Mechoso (2003) identified the periods 36-40, 22-25 and 16-18 days as those of maximum variability of PSA time series derived from 200-hPa streamfunction anomalies over the South Pacific. As we show below, the matching of the dominant periods of IS FOLR variability in SESA and those of PSA variability is not coincidental.

Standard deviations of the 10-90-day filtered geopotential height anomalies at 250 hPa were computed in order to describe the IS variability of the SH circulation (Figure 2). Maximum values are observed along 60°S, with peaks over the southeastern Pacific and southwestern Atlantic Oceans. These values are larger than those observed in the warm season at 60°S (not shown). It is noteworthy that the region

of maximum mean variability on IS time scales does not match that of the storm-tracks (associated with synoptic-scale waves with periods shorter than 10 days) that extends from the southern Atlantic Ocean to the southern Indian Ocean (e.g., Trenberth 1991).

Unlike the geopotential height, meridional wind equally weights circulation changes at every latitude and thus is a useful variable to describe hemispheric circulation variability (e.g., Berbery and Vera 1996). The standard deviation of the 10-90 day filtered meridional wind anomalies at 250 hPa is shown in Figure 3. Two regions of maximum values are evident, one at subpolar latitudes ($\sim 60^{\circ}\text{S}$) over the Pacific Ocean, which was also evident in the geopotential field, and the other one along subtropical latitudes ($\sim 30^{\circ}\text{S}$), extending from Australia to 120°W that is not discernible in the geopotential heights (Figure 3). The band of maximum meridional wind IS variability in the subtropical South Pacific coincides with the subtropical jet region. On the other hand, the IS variability maximum at high latitudes is extended over the Pacific Ocean, eastward of the subpolar jet core exit region located over the Indian Ocean (not shown). This suggests that different mechanisms may be maintaining the IS perturbations at both subtropical and subpolar latitudes. Standard deviation maps of both filtered geopotential heights and meridional winds at 850 hPa were also calculated (not shown). For both variables, the IS variability maximum located over the southeastern Pacific is the only one observed at low levels at approximately the same location as for the 250-hPa circulation anomalies, although with smaller values than at the upper levels.

CSIS activity and associated circulation

The first two leading EOF patterns of FOLR are displayed in Figure 4. The first (CSIS) pattern, which explains 20.7% of the variance, shows a large center of action extended mainly over northern Paraguay, and southern Brazil, and a weaker center of opposite sign located equatorward (Figure 4a). On the other hand, the second EOF, explaining 13.4% of the variance, shows a main center east of Uruguay and another center of opposite sign extending into the tropical Amazon (Figure 4b). The northwest-southeast tilt of these patterns is also typical of prominent intraseasonal patterns in the warm season (e.g., Nogués-Paegle and Mo 1997; Liebmann et al. 1999; González et al. 2008), and consistent with a relationship to equatorward propagating Rossby wave energy (e.g., Berbery et al. 1992).

The criterion developed by North et al. (1982), considering a typical IS period of 45 days (Kessler 2001), was used to test whether these two EOFs are independent or whether they form a degenerate pair. Figure 5 shows that the eigenvalue's error bars corresponding to EOF1 and EOF2 do not overlap and thus appear to be significantly different from each other. Timescales of the PC1 (CSIS index) and PC2 were estimated using power spectra (not shown). CSIS exhibits maximum variability at around 34, 16 and 11 days, while PC2 at around 25 and 12 days. Nevertheless, the spectrum peaks seem to be quite sensitive to small changes in the time series (and none are deemed significant).

During winter, low values of OLR can be related to other phenomena besides convection, such as cooling of land surface temperature or the presence clouds (Kousky and Kayano 1994). Therefore in order to assess if the IS oscillations described by OLR anomalies are also present in precipitation anomalies, lagged regression maps of daily anomalies of both OLR and precipitation over South America were computed against the CSIS index. Figure 6 shows the evolution of both OLR and LA05 precipitation regressed anomalies from 8 days before to 8 days after the CSIS peak, which by design occurs at Day 0. Positive values of regressed precipitation anomalies are associated with days with above-average precipitation. Throughout the entire sequence, positive (negative) precipitation anomalies are associated with negative (positive) OLR anomalies. On Day -8, a center of negative precipitation anomalies extends over SESA that subsequently weakens and eventually is replaced by a positive precipitation anomaly center that is well-developed by Day -2 and peaks on Day 0. By that day negative precipitation anomalies are observed over northeastern South America. On Day 0, the whole pattern resembles, as expected, the one associated to CSIS (Figure 4a). During the following days, the precipitation anomaly maximum weakens while slowly moving northeastward along the coast. Also, after Day +4 a region of negative precipitation anomalies develops over SESA that is evident even at Day +8. The alternation of negative, positive and then negative precipitation anomalies over SESA along the full evolution seems to indicate the predominance of an oscillation with dominant period of around 17 days in association to CSIS activity. For the warm season, Nogués-Paegle and Mo (1997) found, using a compositing technique, that the timescale for the convective anomalies to complete a cycle in South America is also approximately 20 days. The fact that CSIS evolution is clearly discernible in both OLR and precipitation anomalies confirms the ability of the CSIS index to describe the main features of the IS variability in South America.

Figure 7 shows the evolution of regressed anomalies of 250-hPa wind anomalies, along with its divergence, and 500-hPa vertical motion (ω). On Day -8, a NW-SE tilted anticyclonic circulation located in central Argentina is accompanied with upper-level divergence and mid-level ascent on its western flank, while convergence and a small area of mid-level descent is observed mainly over Southern Brazil to its east. On Day -6, a cyclonic circulation is observed off the coast of central Chile, with an associated region of ascent and divergence over central and northern Argentina. In the following days, the cyclonic circulation moves into Argentina, accompanied by increasing upward vertical velocity to the northeast. On Day 0, the cyclone is centered over Argentina while both upper-level divergence and strong ascent correspond to the maximum positive precipitation anomalies (Figure 6) and the center of action of the CSIS pattern (Fig. 4a). In addition, upper-level convergence is observed off the coast of central Chile and over Patagonia to the east of a new anticyclonic circulation center moving from the west. On Day +2, strongest ascent is over southwestern subtropical Atlantic Ocean, and descent intensifies over Uruguay and central Argentina. On the following days the circulation pattern weakens while it continues northeastward. A composite at 850 hPa (Figure 8) reveals that the peak of low-level wind convergence in southern Brazil is on Day -4 before the peak on Day 0 of both ascent and precipitation anomalies. Thus it appears that during the cold season the upper-level circulation seems to be more important than the low-level circulation in inducing the positive precipitation anomalies over SESA.

The evolution of OLR regressed anomalies from 14 prior to 4 days following the peak (in intervals of two days) of CSIS index, is displayed in Figure 9. On Day -14, a center of negative OLR anomalies is located at around 86°W, 35°S. This negative center, although weak, is denoted with an 'X' since this is the center that will develop into the maximum over Paraguay and SE Brazil at Day 0. Also, on Day -14, negative anomalies are evident over the equatorial Indian and Pacific Oceans towards Australia while positive anomalies are discernible over Africa. The evolution of these two features in the following days resembles the composite of the suppressed phase of the northern summer Madden-Julian Oscillation (MJO, e.g., Lawrence and Webster 2002). On Day -12, negative anomalies are still observed over the equatorial and subtropical sector in the vicinity of Australia. On that day, alternate centers of positive and negative anomalies can be identified at the southeastern Pacific Ocean, in which the X center, now at 80°W, 38°S, is embedded. On the following days, the development of these centers becomes more relevant.

On Day -8, positive anomalies extend along the Equatorial Indian Ocean while the companion negative anomalies, located eastwards, have weakened considerably. A negative anomaly region still persists east of Australia that seems to be linked to the alternate centers observed along the south Pacific region. In addition, on Day -8, the X center is off the Chilean coast; positive anomalies intensify over Paraguay and southeastern Brazil, while negative anomalies still persist over northeastern South America. On Day -6, a slow northeastward progression of these three anomaly centers over South America is discernible.

On Day -4, positive anomalies persist in the Equatorial Indian Ocean while alternate anomalies extend between Australia and the southeastern Pacific Ocean upstream of center X, being more intense those closer to South America. In addition center X intensifies and stalls over SESA while the two centers located equatorward over tropical South America weaken. On Day -2, center X continues its intensification, peaking on Day 0, when it extends with a NW-SE orientation over subtropical South America. Also, on Day 0, positive anomalies at both sides of center X continue, while over the Equatorial Indian and western Pacific Oceans the positive anomalies have weakened considerably. Between Day 0 and Day +4, center X remains in the same position, while it weakens.

In summary, the evolution of the OLR regressed anomalies against the CSIS index (Figure 9), confirms that the CSIS pattern development in SESA is accompanied by the evolution of centers of OLR anomalies of alternate sign extended between South America and Australia along the South Pacific Ocean. Also, some evidence of MJO-like eastward progression of OLR anomalies along the Equatorial Indian and Pacific sector is observed.

Regression maps of geopotential height anomalies against the CSIS index were calculated between the levels of 1000 and 100 hPa, and between lags -20 and +20. Vertical cross-sections of the regression (not shown) were used to identify the level of maximum signal, which is at approximately 250 hPa. Figure 10 shows the corresponding regression maps for 250-hPa geopotential height anomalies from 20 days prior and 8 following the CSIS index peak. On Day -20, a cyclonic anomaly over Antarctica and three centers of anticyclonic anomalies in middle latitudes are evident, resembling the positive phase of the SAM in association to a weak but still discernible wave number 3-4 pattern at middle latitudes. During the next few days, SAM-like pattern weakens while, on Day -14, a PSA-like wavetrain starts to develop with positive and

negative anomalies alternating from Australia to South America. The wave train resembles the negative phase of PSA1 identified by Mo and Higgins (1998), as associated with positive (negative) OLR anomalies in the tropical Indian Ocean (Maritime Continent). In particular the cyclonic anomaly located at 110°W, 45°S has been identified as center 'Y', as it will be the one maximizing on Day 0 over northern Argentina, Uruguay and SE Brazil in association with the CSIS peak.

On Day -12, the centers, particularly those over the southeastern Pacific, get more defined as they move slightly eastwards. The pattern observed seems to resemble the PSA2 on its negative phase (Mo and Higgins 1998). On Day -10, the development of a pattern similar to that associated with SAM negative phase starts to develop, with a wavenumber 4 signature at midlatitudes. During this and the following days, both the Y center, as well as the anticyclonic one located upstream, intensify considerably.

On Day -8, two different wavetrains can be identified from Australia to 120°W: one along subtropical latitudes and another along subpolar latitudes. They appear to merge into a single train over the southeastern Pacific. The two wave trains with primarily zonal propagation can be identified west of 120°W, with opposite signed centers at the same longitude. On the other hand, east of 120°W, both wavetrains merge and the centers with large NW-SE tilt penetrate into South America. On Day -6, the pattern resembles along the South Pacific a positive PSA 1 phase (Mo and Higgins 1998), while circulation anomalies over southeastern Pacific Ocean and South America continue growing. Center Y is located at 80°W, 40°S and progresses into the continent while the anticyclonic anomaly located upstream extends from middle latitudes to the Antarctica Peninsula, where it is discernible until Day +4. On Day -2, the anticyclonic anomaly peaks over the southeastern Pacific Ocean while the Center Y continues growing over the southern tip of the continent with a strong NW-SE orientation, similar to PSA2 positive phase. On Day 0, the Y cyclonic center reaches its minimum value over eastern Argentina, and its eastern flank is coincident with the OLR anomaly associated with CSIS pattern (Figure 8, Day 0). During that day, while circulation anomalies over the western Pacific have weakened considerably, the anticyclonic anomaly center located over the southeastern Pacific Ocean remains considerable. On this day, the regression pattern is similar to the negative PSA 1, which shows negative geopotential heights anomalies over SESA and an anticyclonic NW-SE-tilted center upstream, extending from subtropical latitudes of the eastern Pacific Ocean to the Antarctica Peninsula.

From days +2 until +8, the anticyclonic anomaly located upstream of Y center continues its northeastward progression while the Y center moves eastward while decreasing in strength. On Day +4, the pattern has evolved into a negative PSA 2 phase with the Y center progressing further north. On Day +8, the anticyclonic anomaly upstream of the Y center reaches the same position that Y center had on Day 0. In the following days, the regression signal is considerably weaker.

The presence of a quasi-stationary anticyclonic anomaly west of the Antarctica Peninsula in association to the development of positive precipitation anomalies over SESA on IS timescales has been also identified by Solman and Orlanski (2010). They found that precipitation anomalies in SESA during the austral spring are associated with the presence of an anomalous quasi-stationary anticyclonic circulation over southeastern Pacific Ocean. They showed that ten days before to the SESA precipitation maximum, the anticyclonic anomaly is located at subpolar latitudes and at around 135°W, while on the maximum precipitation day, the anticyclonic anomaly is over the Bellingshausen Sea, extended to the northwest.

Throughout the sequence displayed in Figure 10, it is evident that energy is dispersed along a great circle route resulting in the tilted wavetrain pattern over SESA associated with the CSIS pattern. Moreover, the progression from PSA1 negative phase, to PSA2 negative phase, to PSA1 positive phase, to PSA2 positive phase, and so on, described by the regression maps based on CSIS activity is the evolution identified by Mo and Higgins (1998) as dominant between PSA1 and PSA2. The latter confirms the large impact of the leading patterns of IS variability of SH circulation onto the CSIS activity in South America. Nevertheless, the analysis of Figure 10 also shows influence of SAM activity in association with clear wavenumber 3-4 patterns, which has not been identified in previous work (e.g., Mo and Higgins 1998; Kidson 1999) as dominating the IS variability of the SH circulation.

CSIS activity and daily precipitation events

The comparison between the evolution of CSIS index and that of SESA daily precipitation series (defined in section 2b), shows that daily precipitation seems to be largely modulated by CSIS activity. As an example, the evolution of daily amounts derived from SESA precipitation time series and that of CSIS index for the 1986 cold season is presented in Figure 11. Consecutive days of precipitation alternate with periods of little or no rain, and episodes of rainfall mainly lie within periods of positive CSIS index. A similar behavior

is observed in most of the other years from the period of study as well (not shown). In agreement, Gonzalez et al. (2008) showed that the leading pattern of IS variability during the warm season strongly modulates daily precipitation in SESA.

4228 days lie within the 28 cold seasons considered here, and 1209 of which registered measurable precipitation (at least 1 mm). Moreover, around 85% of those days correspond to wet spells (defined in section 2b) of duration 2 to 11 days, while around 15% of them are isolated daily events.

Wet spells in SESA were classified according to the CSIS phase within which they occurred. The classes considered were: *wet* (CSIS positive phase), *dry* (CSIS negative phase), *wet-to-dry* and *dry-to-wet*. The last two categories correspond to those wet spells occurring in periods including CSIS sign changes from either positive to negative or the other way around. If wet spells that lasted 4 days or more occurred mostly within a certain CSIS phase excepting for one day of the wet spell, they are classified under that predominant CSIS phase. For example, a wet spell of 7 days of duration in which 6 days occurred in a positive CSIS phase is classified as a spell under the *wet* category. Figure 12 shows the climatological distribution of wet spells and P75 wet spells that lasted between 2 and 7 days, accordingly to the CSIS phase in which they occurred. Longer wet spells were rarely observed (see Table 2) and thus they are not shown. Figure 12a shows clearly how favorable it is for wet spells to occur while CSIS is in a positive phase. For wet spells lasting 2 days, 58.7% occurred in wet CSIS phases and 26.3% in dry CSIS phases. This difference becomes larger as wet spell duration increases. For example, 84.4% (9.4%) of wet spells lasting 4 days, occurs in CSIS wet (dry) phases. Figure 12a also shows that neither wet spells of 6 days of duration nor those of 7 days occur in dry or wet-to-dry categories.

The analysis of the occurrence of P75 wet spells (defined in section 2b) shows that 306 P75 wet days are identified in the 28 cold seasons; around 45% of them occurred as 57 P75 wet spells, and around 55% as isolated daily events. Moreover, almost 80% of the P75 wet spells last for two days (Table 2). One unusual event is a P75 wet spell that lasted 8 days during 1983. In addition, Figure 12b shows the largest percentage of P75 wet spells are associated with CSIS wet phases, representing up to 80% of those lasting 2 days. Only three P75 wet spells of 4-day duration occurred, with two of them in CSIS wet phases and one in a dry-to-wet period.

To better understand the influence of CSIS evolution on wet spells, those of 4 days of duration were selected and further analyzed. Wet spells of that duration were chosen because they are representative of long wet spells and they have occurred 32 times in the period under study (Table 2), which is a number large enough that composites are usually determined to be statistically significant. Composites of daily CSIS index values were performed on the basis of the 32 events of 4-day wet spells. Day 0 corresponds to the starting day of the wet spell. Figure 13 shows the mean CSIS index values from Day -9 to Day +3, along with the dispersion represented as a box plot. Between Days 0 and +3 that correspond to the 4-day wet spell duration, CSIS mean values are significantly positive (wet phase) and have mean CSIS index values larger than one standard deviation. The latter reflects the intensity of the CSIS wet phase during the wet spell. The maximum value of the CSIS index is reached, on average, on the third day of the wet spell. On the other hand, from Day -1 backward, CSIS composite values decrease becoming around 0 on Day -3 and reaching a minimum value on Day -5, although the dispersion among the results obtained from the set of 4-day wet spell events is large.

Composites of 250-hPa geopotential height anomalies were computed on the basis of the 32 events of 4-day wet spell (Fig. 14). Wet spells are seen to occur in association to the development and persistence of a large cyclonic anomaly over extratropical and subtropical South America. Such an anomaly is related to circulation anomalies of alternate sign mainly in the South Pacific similar to PSA wavetrains. A comparison between the circulation anomaly patterns associated with 4-day wet-spells in SESA (Fig. 14) and those associated to CSIS evolution (Fig. 10) was made. In order to facilitate this, Day 0 in Figure 14 corresponds to the third day of the 4-day wet spell which in average represents the CSIS peak (Fig. 13). The comparison shows large similarities in the phase evolution of the PSA-like patterns along the South Pacific, and evidence of a negative SAM index as well as in the main features of the circulation anomalies in the vicinity of South America. In particular, a ‘Y’ anticyclonic center, equivalent to that defined for CSIS related circulation anomalies (Figure 10) can be traced in the composites for wet spells since Day -10, acquiring a strong identity between days -4 and +2 (Figure 14). In addition, a cyclonic anomaly develops in both cases over South America. However, its propagation seems to be slower in the composite for the wet spells, which might favor the consecutive days of precipitation in SESA.

Finally, the CSIS possible influence on daily precipitation extremes in SESA (defined in section 2b), is explored. Table 3 shows that more than 80% of the daily precipitation extremes occur during a CSIS wet phase. Composites of daily CSIS index values were performed on the basis of the daily precipitation extreme occurrence. Day 0 corresponds to the daily extreme date. Figure 15 shows the mean CSIS index values and dispersion from Day -4 to Day +2. The behavior of the index is similar for type of daily extremes defined by the 90th (Fig. 15a) and 99th (Fig. 15b) percentiles. The mean CSIS index turns positive at around 3 days before the occurrence of the extreme event, and approaches one standard deviation on the day prior to the extreme event, remaining so on the two following 2 days at least.

Discussion and Conclusions

The IS variability in South America during the cold season is documented in this paper. IS variability, as described by 10-90 day bandpass filtered OLR anomalies, explains a large percentage of the OLR variance over South America during that season. FOLR standard deviation exhibits maximum values over Paraguay and southeastwards. Furthermore, the associated IS variability of the SH circulation shows maximum amplitude along subpolar latitudes of the Pacific Ocean as well as along subtropical latitudes from Australia to 120°W.

The leading pattern of FOLR, or CSIS, as identified by an EOF analysis, is characterized by a monopole extended with a NW-SE orientation over SESA. The analysis of the CSIS influence on both precipitation and OLR anomalies in South America shows the alternation of wet and dry periods in SESA with a dominant period of around 17 days in association to CSIS activity.

The analysis of the large-scale conditions shows that OLR anomalies associated with CSIS evolution resemble those linked to boreal summer MJO-like activity over the tropical Indian and west Pacific Oceans. In addition, large-scale circulation anomalies in the SH associated with CSIS activity exhibit evidence of SAM activity in combination with a wavenumber 3-4 pattern at midlatitudes as well as the development of PSA-like Rossby wavetrains. This result agrees with previous works that describe the IS variability in the SH circulation (e.g., Kidson 1999) and with those focusing their studies over western Antarctica (e.g., Yu et al. 2011). Moreover, the phase evolution of the PSA-like patterns influencing CSIS activity in South America is

very similar to that described by Mo and Higgins (1998) as associated with the leading patterns of SH circulation variability on IS time scales.

At regional scales, the increase of positive precipitation anomalies in SESA due to CSIS phase is favored by the intensification of a cyclonic anomaly center over extratropical South America. Such a cyclonic anomaly is discernible at least 14 days before CSIS peaks over SESA. During that period, the cyclonic center progresses from the southeastern Pacific towards South America while its amplitude increases. The cyclonic center evolution is accompanied by the intensification of an anticyclonic anomaly center located upstream, which during the days prior to CSIS peak is located over the southeastern Pacific and extends poleward over the Antarctica Peninsula. It is speculated that the stationary behavior of that anticyclonic anomaly center located south of South America favors the stalling of the cyclonic center over extratropical South America. Moreover, the fact that the anticyclonic anomaly center at high latitudes remains almost motionless for more than 10 days seems to be favored by a hemispheric circulation anomaly pattern resembling that associated with a negative SAM phase combined with a wavenumber 3-4 pattern. Nevertheless, further research is needed to better understand how much of that IS circulation variability identified here over the SH is forced by tropical convection and how much is due to internal atmospheric variability due to wave-mean flow interaction within the storm tracks.

The analysis of CSIS influence on the character of rainfall events in SESA shows that CSIS activity induces a large modulation of daily precipitation anomalies. In particular, wet (dry) spells are favored during positive (negative) CSIS phases. Composite analyses based on 4-day wet spell occurrence show that they tend to be associated on average with more intense than normal CSIS wet phases. Patterns of circulation anomalies associated with 4-day wet spells occurrence are very similar those identified as associated to CSIS activity. The latter confirms the relevant role that IS circulation variability has in both the SH, and in particular, South America, in promoting long wet spells in SESA. The analysis of P75 wet spells (or those associated with consecutive days with daily rain amount above the 75th percentile value) gives similar results indicating the important role of CSIS in also modulating the more intense wet spells. The influence of CSIS activity on the occurrence of daily precipitation extremes in SESA shows that more than 80% of them occur during a CSIS

wet phase. We conclude that IS variability is crucial for the development of the regional conditions more favorable to daily precipitation extreme occurrence.

Acknowledgments

This research was supported by CONICET PIP 112-200801-00399, UBACyT 20020100100434, ANPCyT PICT-2010-2110, NOAA Climate Program Office GC10-685 and NA00AR4310170. M.A. is supported by a Ph.D grant from CONICET, Argentina.

References

- Ambrizzi T, Hoskins BJ, Hsu H (1995) Rossby wave propagation and teleconnection patterns in the austral winter. *J Atmos Sci* 52:3661-3672.
- Baba K, Minobe S, Kimura N, Wakatsuchi M (2006) Intraseasonal variability of sea-ice concentration in the Antarctic with particular emphasis on wind effect. *J Geophys Res* 111(12).
- Berbery EH, Nogués-Paegle J, Horel JD (1992) Wavelike Southern Hemisphere extratropical teleconnections. *J Atmos Sci* 49 :155–177; Corrigendum, 49 :2347.
- Berbery EH, Nogués-Paegle J (1993) Intraseasonal interactions between the tropics and extratropics in the Southern Hemisphere. *J Atmos Sci* 50(13):1950-1965
- Berbery EH, Vera CS (1996) Characteristics of the Southern Hemisphere winter storm track with filtered and unfiltered data. *J Atmos Sci* 53(3):468-481.
- Cerne SB, Vera CS (2011) Influence of the intraseasonal variability on heat waves in subtropical South America. *Clim Dyn* 36(11-12):2265-2277.
- Duchon CE (1979) Lanczos filtering in one and two dimensions. *J of Appl Meteorol* 18(8):1016-1022.
- Ghil M, Mo KC, (1991) Intraseasonal oscillations in the global atmosphere. Part II: Southern Hemisphere. *J Atmos Sci* 48(5):780-790.
- González PLM, Vera CS, Liebmann B, Kiladis GN (2008) Intraseasonal variability in subtropical South America as depicted by precipitation data. *Clim Dyn* 30(7-8):727-744.
- Kalnay E et al (1996) The NCEP/NCAR 40-year reanalysis project. *Bull of the Am Meteorol Soc* 77(3):437-471.
- Kessler WS (2001) EOF representations of the Madden-Julian oscillation and its connection with ENSO. *J of Clim* 14(13):3055-3061.
- Kidson JW (1999) Principal modes of Southern Hemisphere low-frequency variability obtained from NCEP-NCAR reanalyses. *J of Clim* 12(9):2808-2830.
- Kousky VE, Kayano MT (1994) Principal modes of outgoing longwave radiation and 250-mb circulation for the south american sector. *J of Clim* 7(7):1131-1143.
- Lawrence DM, Webster PJ (2002) The boreal summer intraseasonal oscillation: relationship between northward and eastward movement of convection. *J Atmos Sci* 59:1593-1606.

- Liebmann B, Allured D (2005) Daily precipitation grids for South America. *Bull of the Am Meteorol Soc* 86(11):1567-1570.
- Liebmann B, Kiladis GN, Marengo JA, Ambrizzi T, Glick JD (1999) Submonthly convective variability over South America and the South Atlantic convergence zone. *J of Clim* 12:1877-1891.
- Liebmann B, Smith CA (1996) Description of a complete (interpolated) outgoing longwave radiation dataset. *Bull of the Amer Meteorol Soc* 77:1275-1277.
- Liebmann B, Vera CS, Carvalho LMV, Camilloni IA, Hoerling M, Allured D, Barros V, Baez J, Bidegain M (2004) An Observed trend in central south american precipitation. *J Clim* 17:4357-4367.
- Liebmann B, Kiladis GN, Vera, CS, Saulo AC, Carvalho LMV (2004) Subseasonal variations of rainfall in South America in the vicinity of the low-level jet east of the andes and comparison to those in the South Atlantic Convergence Zone. *J of Clim* 17(19):3829-3842.
- Mo KC, Ghil M (1987) Statistics and dynamics of persistent anomalies. *J Atmos Sci* 44:877-902.
- Mo KC, Higgins RW (1998) The Pacific-South American modes and tropical convection during the Southern Hemisphere winter. *Mon Weather Rev* 126(6):1581-1596.
- Nogués-Paegle J, Mo KC (1997) Alternating wet and dry conditions over South America during summer. *Mon Weather Rev* 125(2):279-291.
- North GR, Bell TL, Cahalan RF, Moeng FJ (1982) Sampling errors in the estimation of empirical orthogonal functions. *Mon Weather Rev* 110:699-706.
- Peterson TC et al (2001) Report on the activities of the working group on climate change detection and related rapporteurs 1998 – 2001. WMO Rep. WCDMP 47, WMO – TD 1071, Geneva, Switzerland 143 pp.
- Robertson AW, Mechoso CR (2003) Circulation regimes and low-frequency oscillations in the South Pacific sector. *Mon Weather Rev* 131:1566-1576.
- Solman SA, Orlanski I (2010) Subpolar high anomaly preconditioning precipitation over South America. *J of Atmos Sci* 67(5):1526-1542.
- Tolika K, Maheras P (2005) Spatial and temporal characteristics of wet spells in Greece. *Theor and Appl Clim*, 81(1-2):71-85.
- Trenberth KE (1991) Storm tracks in the Southern Hemisphere. *J Atmos Sci* 48(19):2159-2178.
- Yu L et al (2011) The intraseasonal variability of winter semester surface air temperature in Antarctica. *Polar Res* doi:10.3402/polar.v30i0.6039
- Zolina O, Simmer C, Kapala A, Gulev S (2005) On the robustness of the estimates of centennial-scale variability in heavy precipitation from station data over Europe. *Geophys Res Lett* 32(14):1-5.

500

Tables

Station Name	Latitude (°S)	Longitude (°W)
Sao Miguel Do Iguaçu	25.18	54.13
Sao Miguel Do Iguaçu	25.35	54.25
Palotina	24.30	59.92
Parque Nacional Iguaçu	25.63	54.48
Salto Cataratas	25.68	54.53
Estreito Do Iguaçu	25.55	53.85
Sao Jose Dos Campos	22.28	57.94
Puerto Casado	22.28	57.94
Concepción	23.44	57.43

TABLE 1 Stations used for constructiong the SESA precipitation time series.

501

	Duration									
	2	3	4	5	6	7	8	9	10	11
WS	179	67	32	22	13	7	2	2	2	1
P75WS	45	8	3	0	0	0	1	0	0	0

TABLE 2 Number of wet spells (WS) and P75 Wet Spells (P75 WS) observed as a function of their duration

502

Extreme event	Threshold (mm)	Observed (times)	Wet phase	Dry phase
90%	30.9	122	100 (82%)	22 (18%)
99%	69.5	12	10 (83%)	2 (17%)

TABLE 3 Descriptive values of precipitation extremes associated to CSIS activity

503

504

505

Figure Captions

Fig. 1 Standard deviation of 10-90 day filtered OLR (FOLR) in South America for (a) cold season (May-September) and (b) warm season (November-March). Contour interval is 2 W m^{-2}

Fig. 2 Standard deviation of 10-90 day filtered 250-hPa geopotential height anomalies in the SH for the cold season. Outer latitude circle is 10°S and the increment is 20° latitude. Contour interval is 18 m/gp

Fig. 3 As in figure 2 but of 10-90 day filtered 250- hPa meridional wind anomalies. Contour interval is 1.5 m s^{-1}

Fig. 4 (a) First and (b) second leading EOF of FOLR for the cold season. Contour interval is 2 (non-dimensional units), negative contours are dashed and 0 contour is omitted

Fig. 5 Percentage of explained variance by each EOF (North et al., 1982). Bars represent the eigenvalue error

Fig. 6 Linear regression maps of precipitation (mm day^{-1} , shaded) and OLR (contours) anomalies against the CSIS index. Contour interval is 2.5 W m^{-2} . Negative contours are dashed, and 0 contour is omitted. Precipitation units are mm day^{-1} . Values displayed are significant at the 95% confidence level

Fig. 7 Linear regression maps of wind anomalies at 250 hPa (m s^{-1} , vectors) and vertical velocity omega anomalies at 500 hPa (contours) against the CSIS index. Contour interval is 0.005 Pa s^{-1} . Negative contours are dashed, and 0 contour is omitted. The divergence of the wind regression is displayed in shaded, with a scale factor of 10^{-7} . Values displayed are significant at the 95% confidence level

Fig. 8 Linear regression maps of wind anomalies at 850 hPa (m s^{-1} , vectors). The divergence of the wind regression is displayed in shaded, with a scale factor of 10^{-7} . Values displayed are significant at the 95% confidence level

Fig. 9 Linear regression maps of OLR anomalies against the CSIS index. Contours increase with a step of 2.5 W m^{-2} . Negative contours are dashed and 0 contour is omitted. Values displayed are significant at the 95% confidence level. The “X” identifies the center that develops into the maximum over Paraguay and SE Brazil at Day 0

Fig. 10 Linear regression maps of 250- hPa geopotential height anomalies against the CSIS index. Contour interval is 5 gpm . Negative contours are dashed and 0 contour is omitted. Outer latitude circle is 10°S and the circle increment is 20° latitude. Values displayed are significant at the 95% confidence level. The “Y” identifies the center maximizing on Day 0 over northern Argentina, Uruguay and SE Brazil

Fig. 11: Evolution of daily rainfall cumulates from SESA precipitation time series (blue bars) and the standardized CSIS index (green line), for 1986 cold season (see text for details).

Fig. 12 Climatological distribution of wet spell (a) and P75 wet spell (b) frequency according to CSIS phases

Fig. 13 Evolution of mean CSIS index values (blue line and circles) and dispersion presented as a box plot computed over all the events of 4-day wet spells identified during CSIS wet phases. The days of wet spell occurrence are from Day 0 to Day + 3. The day in which the wet spell starts is day 0, and it is marked on the horizontal axis. On each box, the central mark is the median, the edges of the box are the 25th and 75th percentiles and the whiskers extend to the most extreme values

Fig. 14 250 hPa geopotential heights anomalies composites for wet spells of 4 days of duration that occurred during a wet phase of CSIS (gpm , shaded and white contours). Negative contours are dashed and 0 contour is omitted. Numbers at the top left of each map indicate the number of lag in days respect

to the day of maximum value of CSIS index, day 0. The wet spell takes place between days -2 and -1, and days within it are marked with an asterisk. Thick black contours indicate significance to the 95% confidence level.

Fig. 15 Evolution of mean CSIS index values (blue lines and circles) and dispersion presented as a box plot over all daily extreme events identified during CSIS wet phases and defined by the (a) 90th and (b) 99th percentile. The day of the extreme event occurrence is day 0, and it is marked on the horizontal axis. On each box, the central mark is the median, the edges of the box are the 25th and 75th percentiles and the whiskers extend to the most extreme values

Figure1
[Click here to download high resolution image](#)

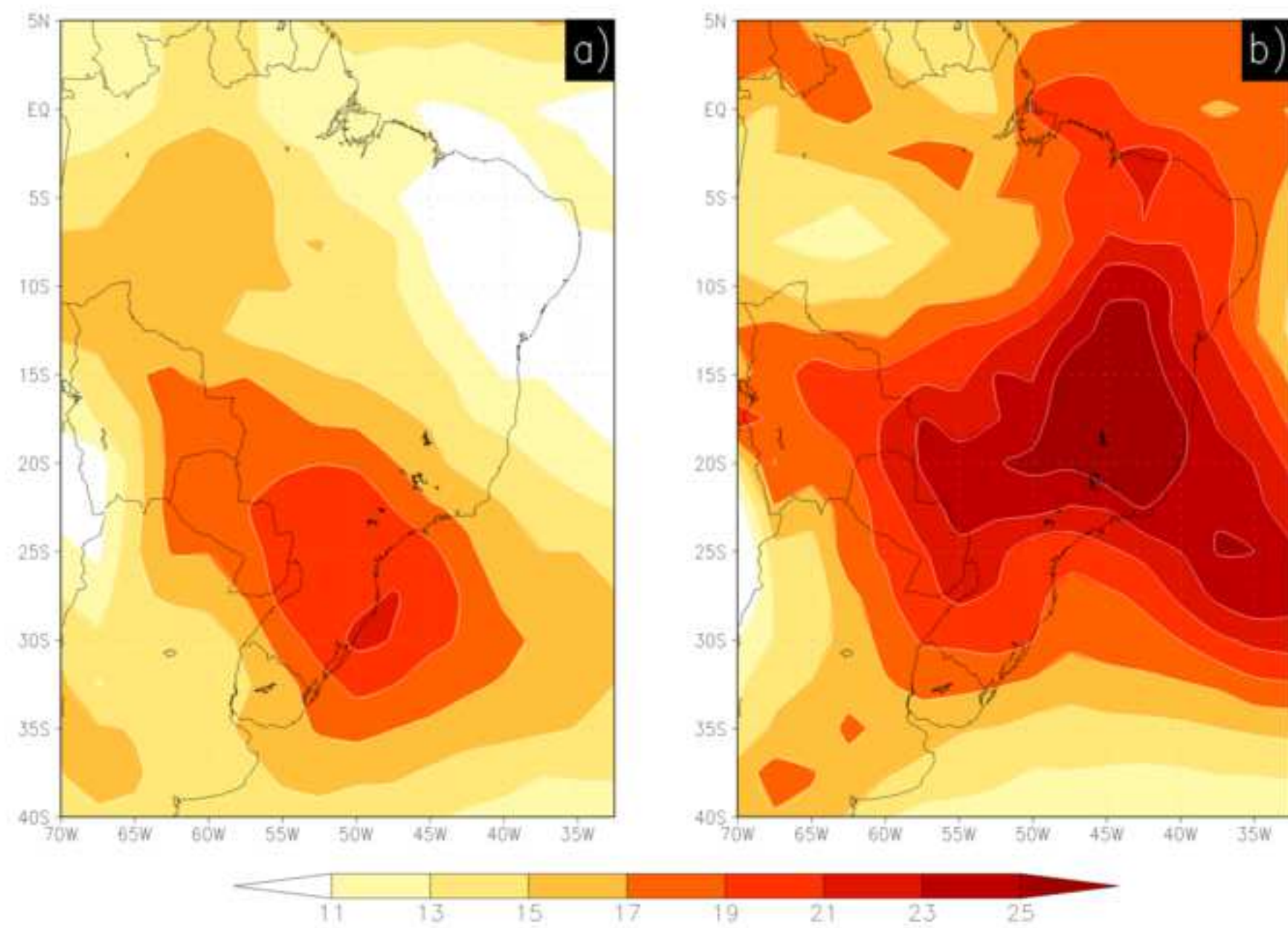


Figure2
[Click here to download high resolution image](#)

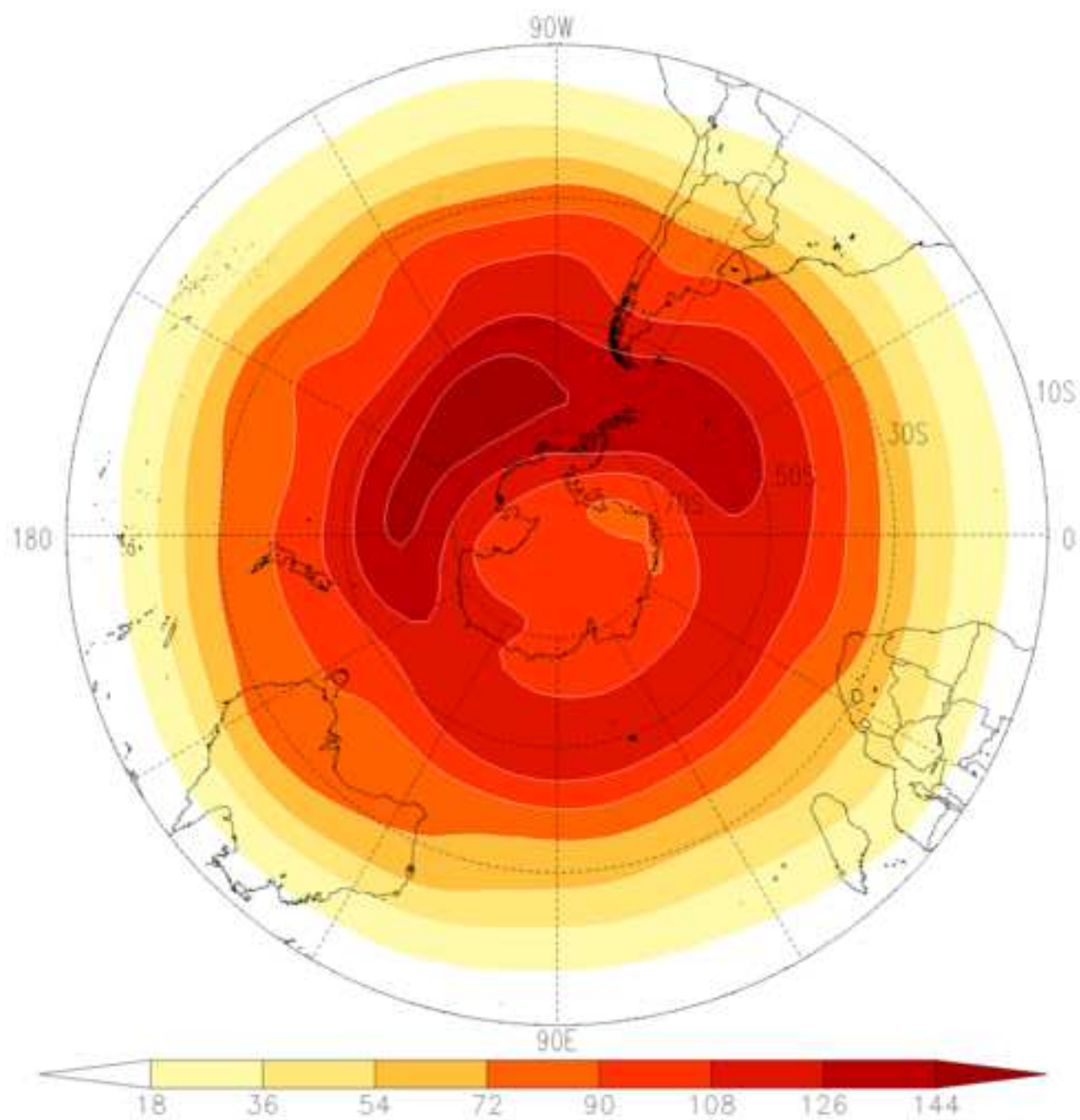


Figure3
[Click here to download high resolution image](#)

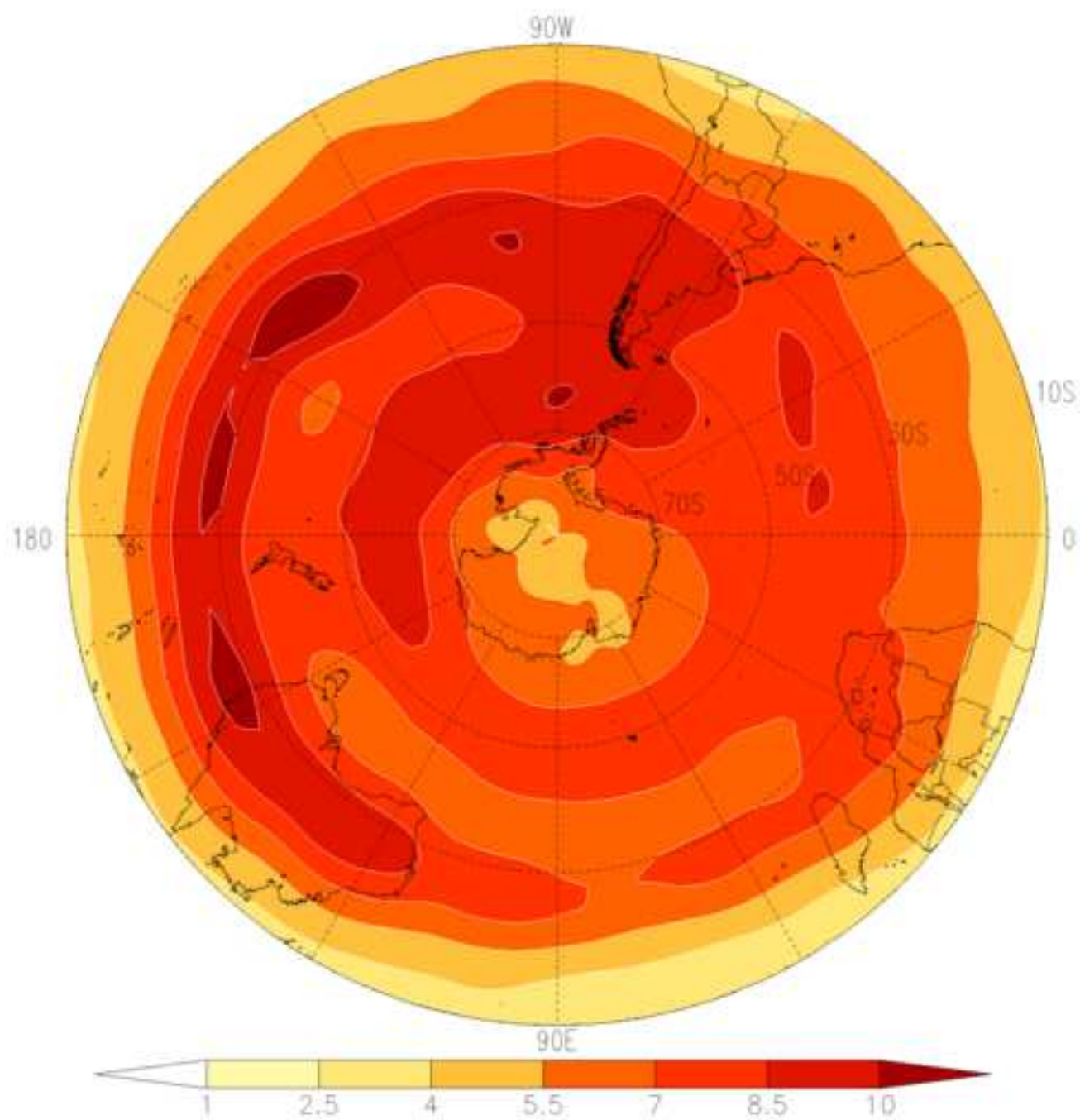


Figure4
[Click here to download high resolution image](#)

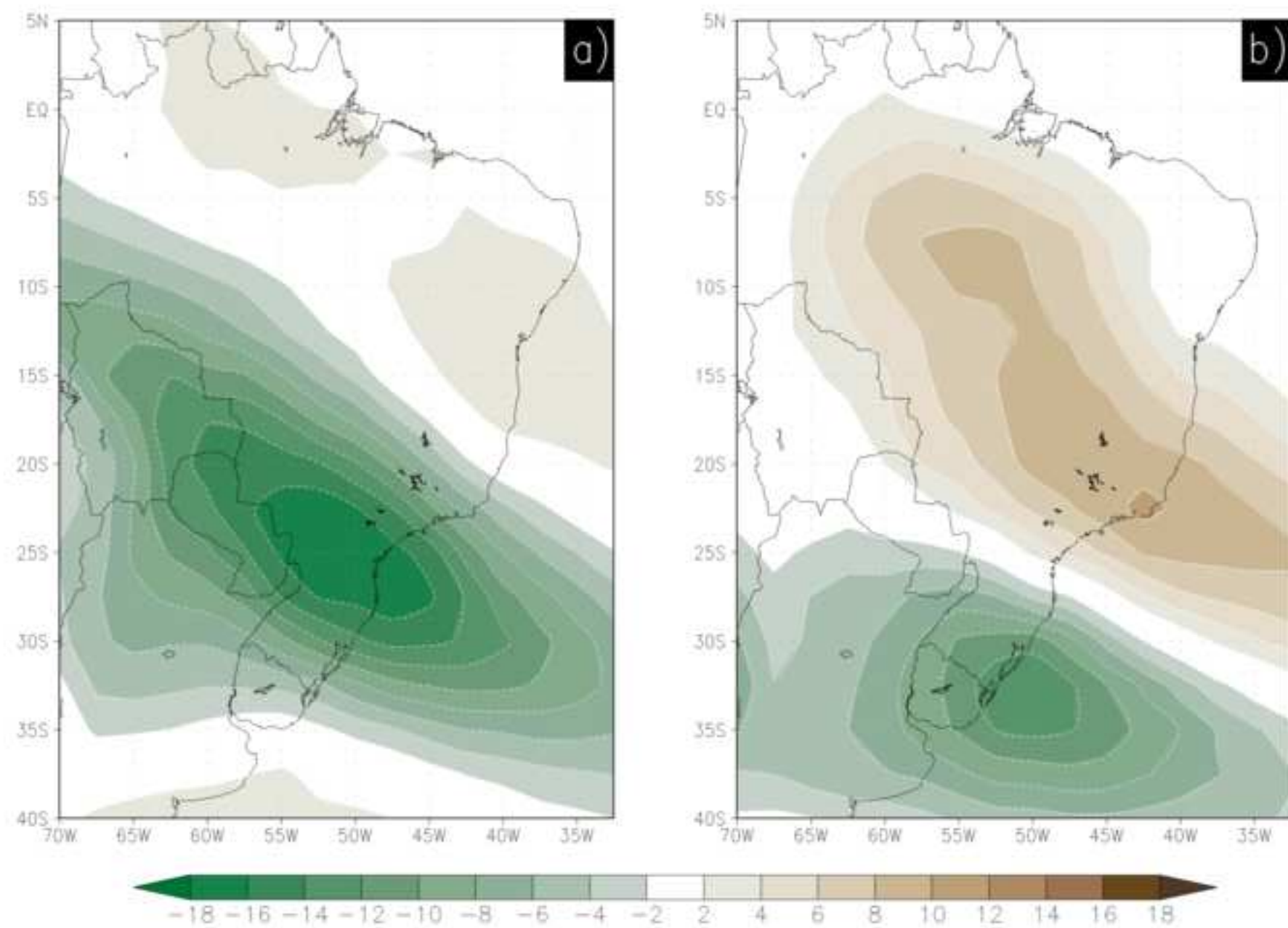


Figure5
[Click here to download high resolution image](#)

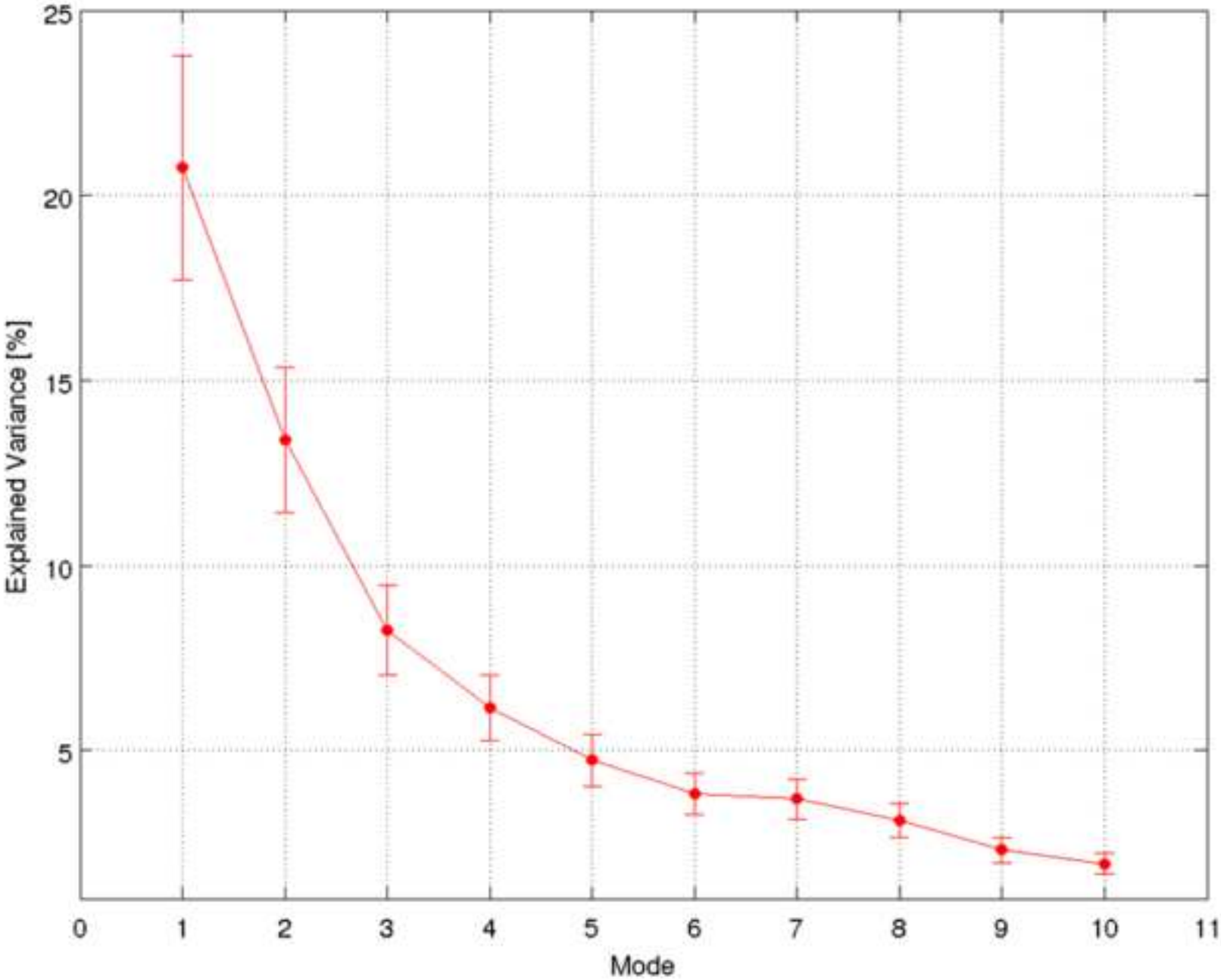


Figure6
[Click here to download high resolution image](#)

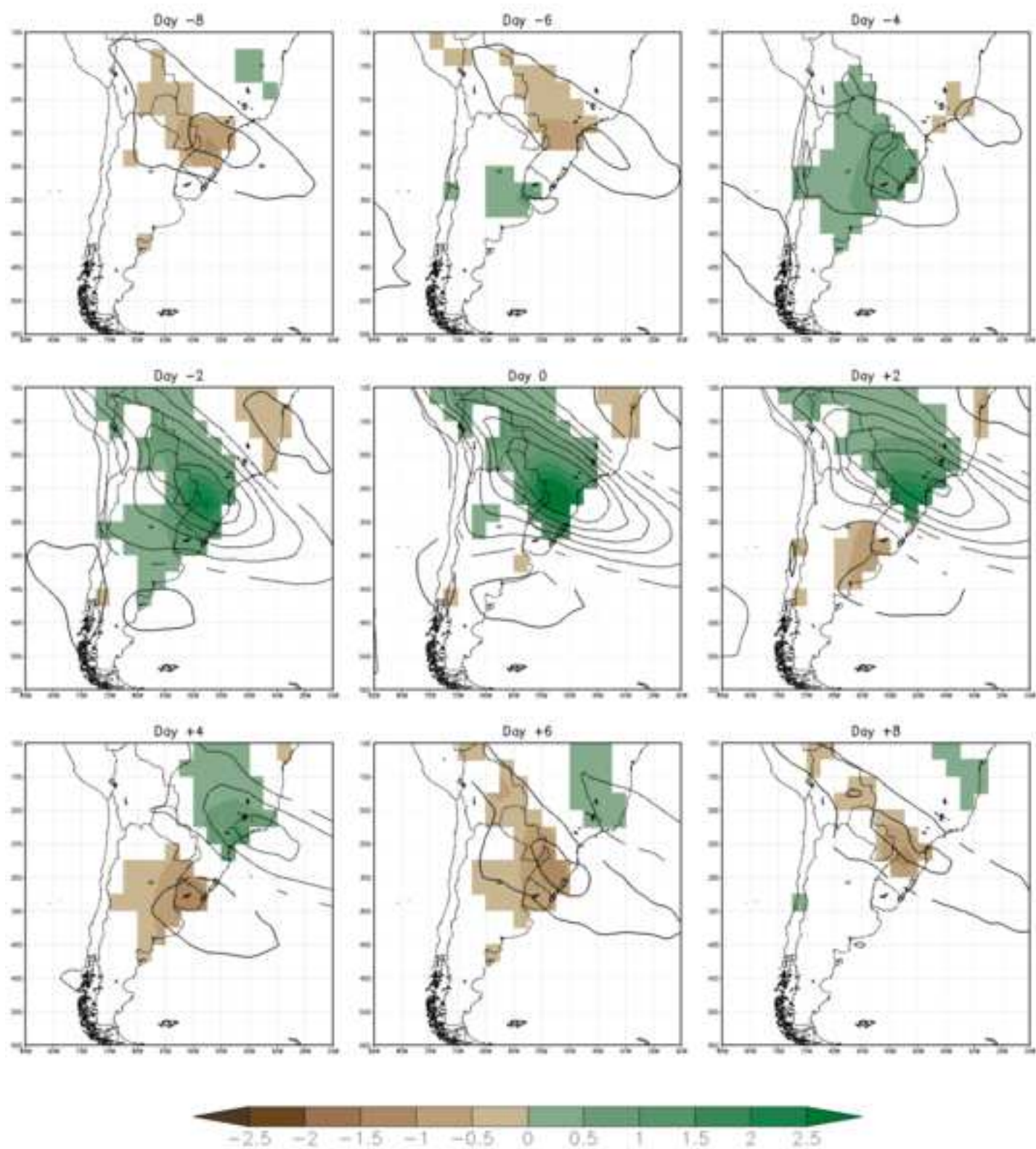


Figure7
[Click here to download high resolution image](#)

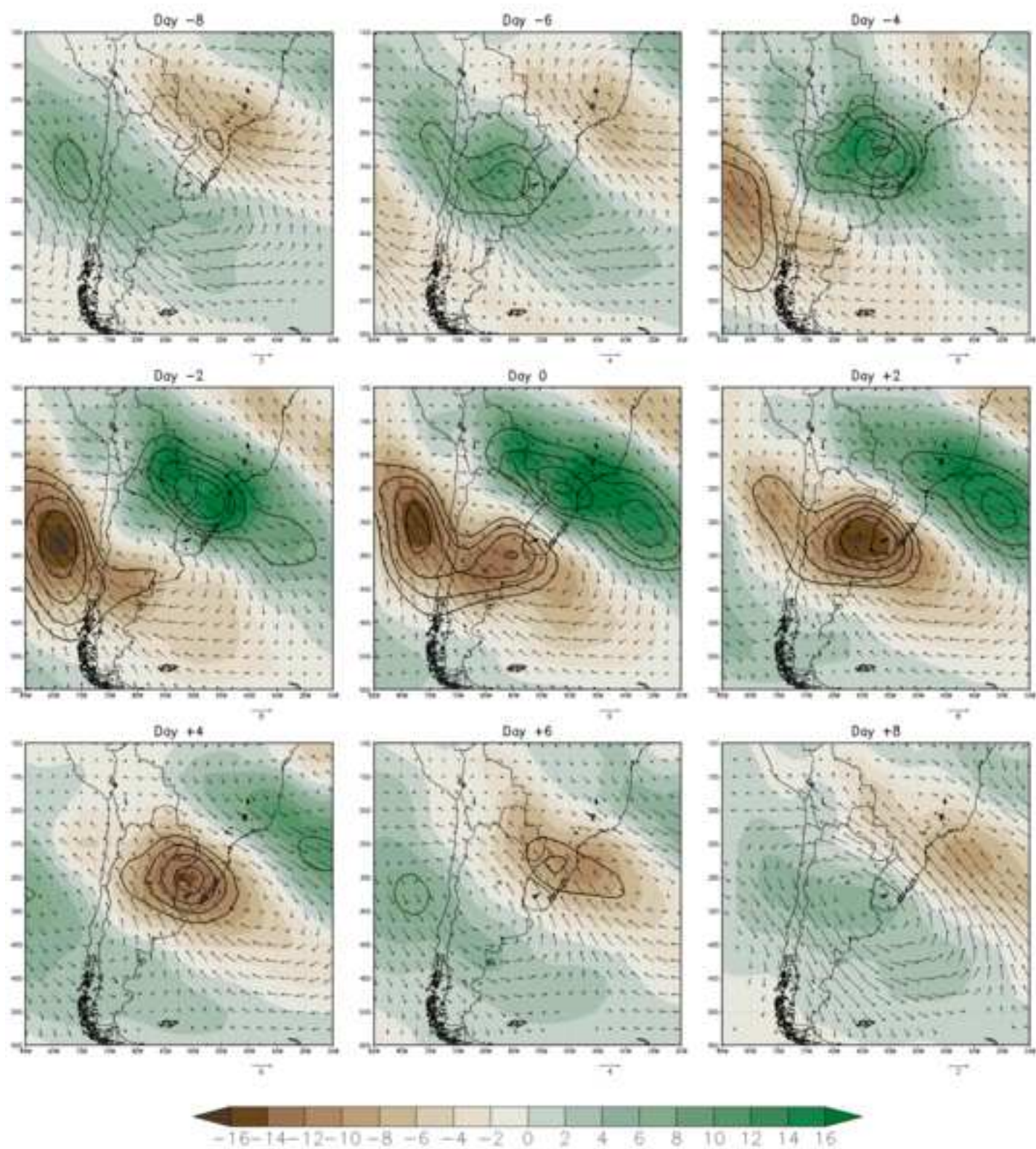


Figure8

[Click here to download high resolution image](#)

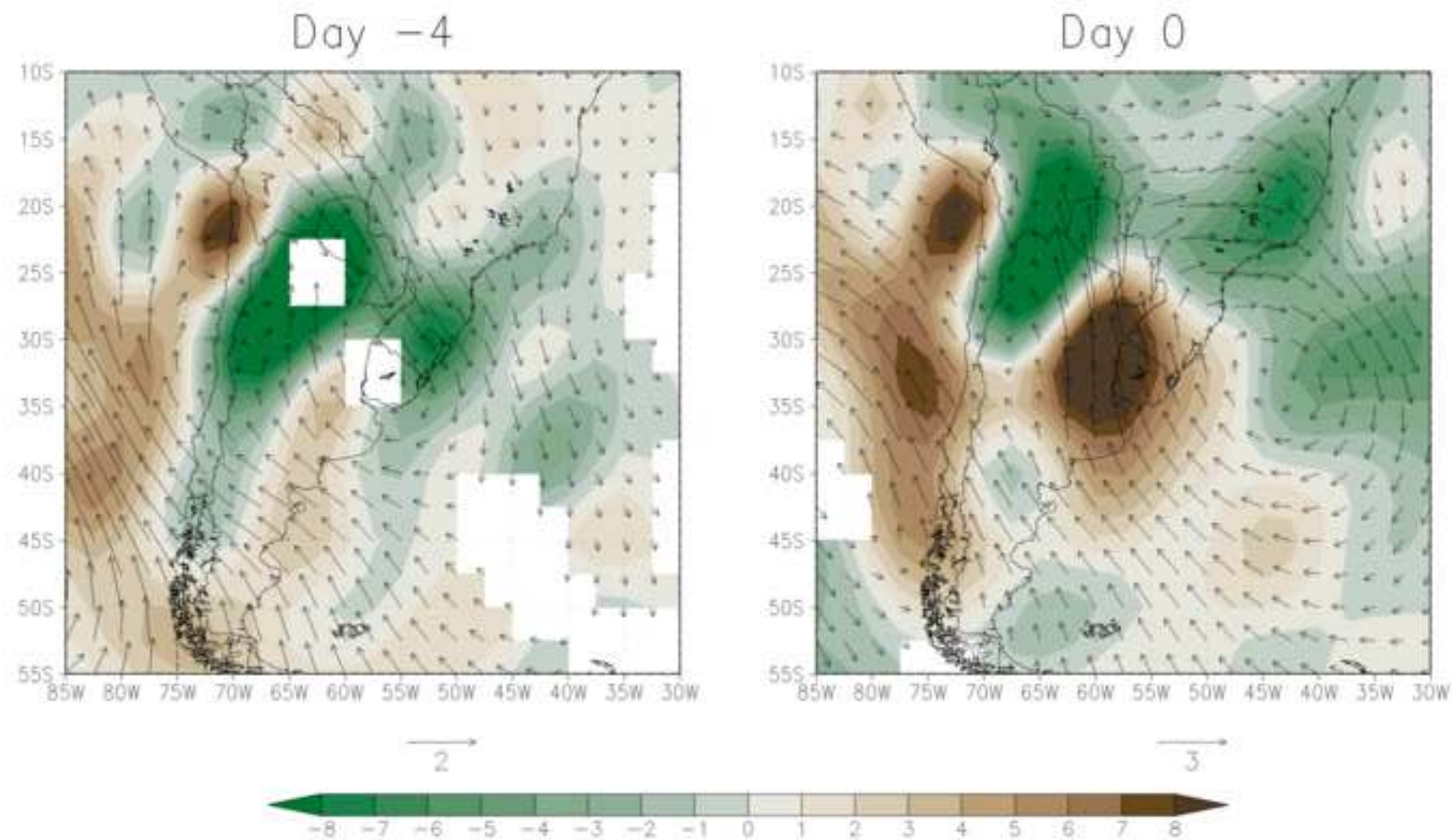


Figure9

[Click here to download high resolution image](#)

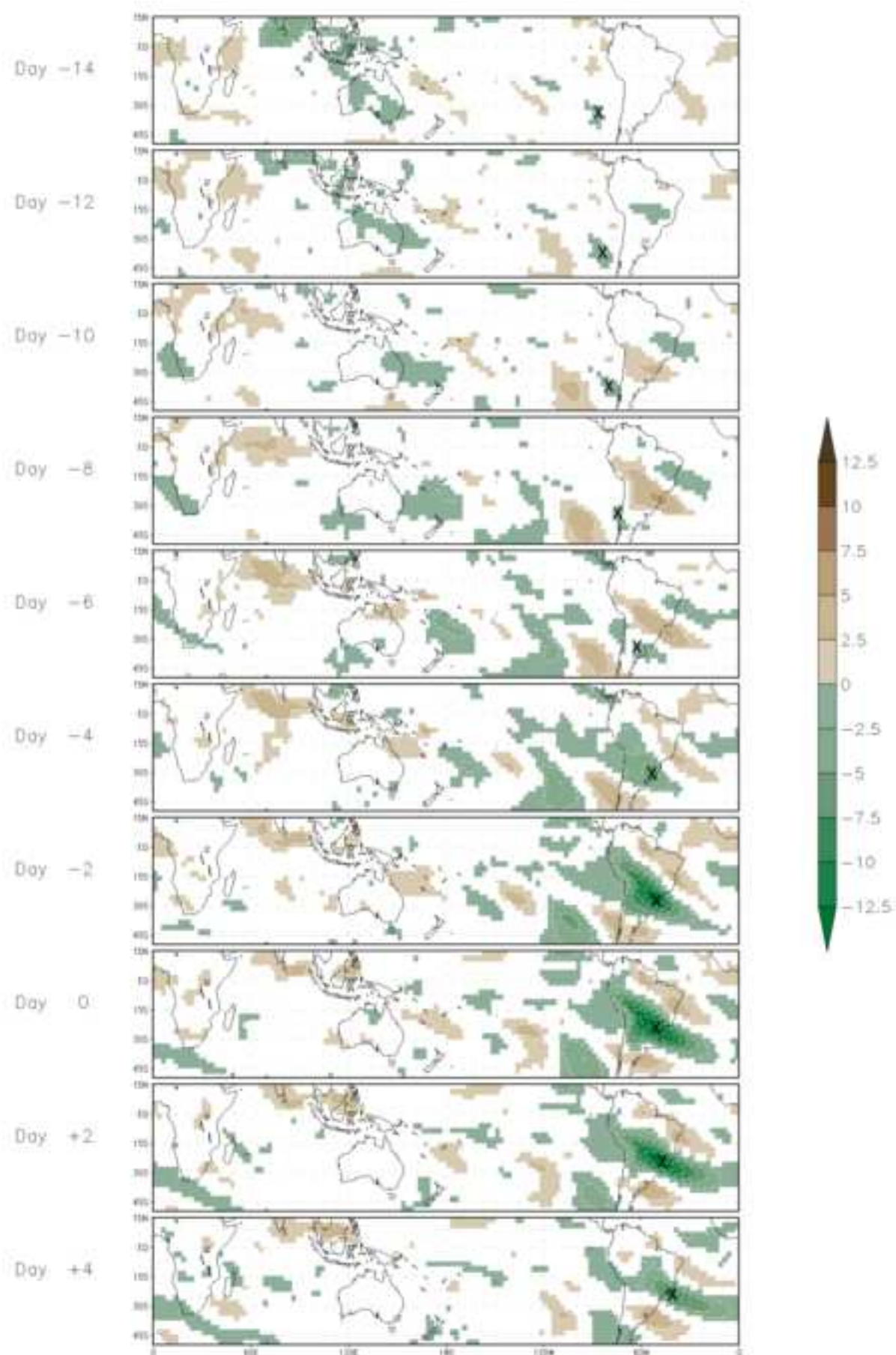


Figure10
[Click here to download high resolution image](#)

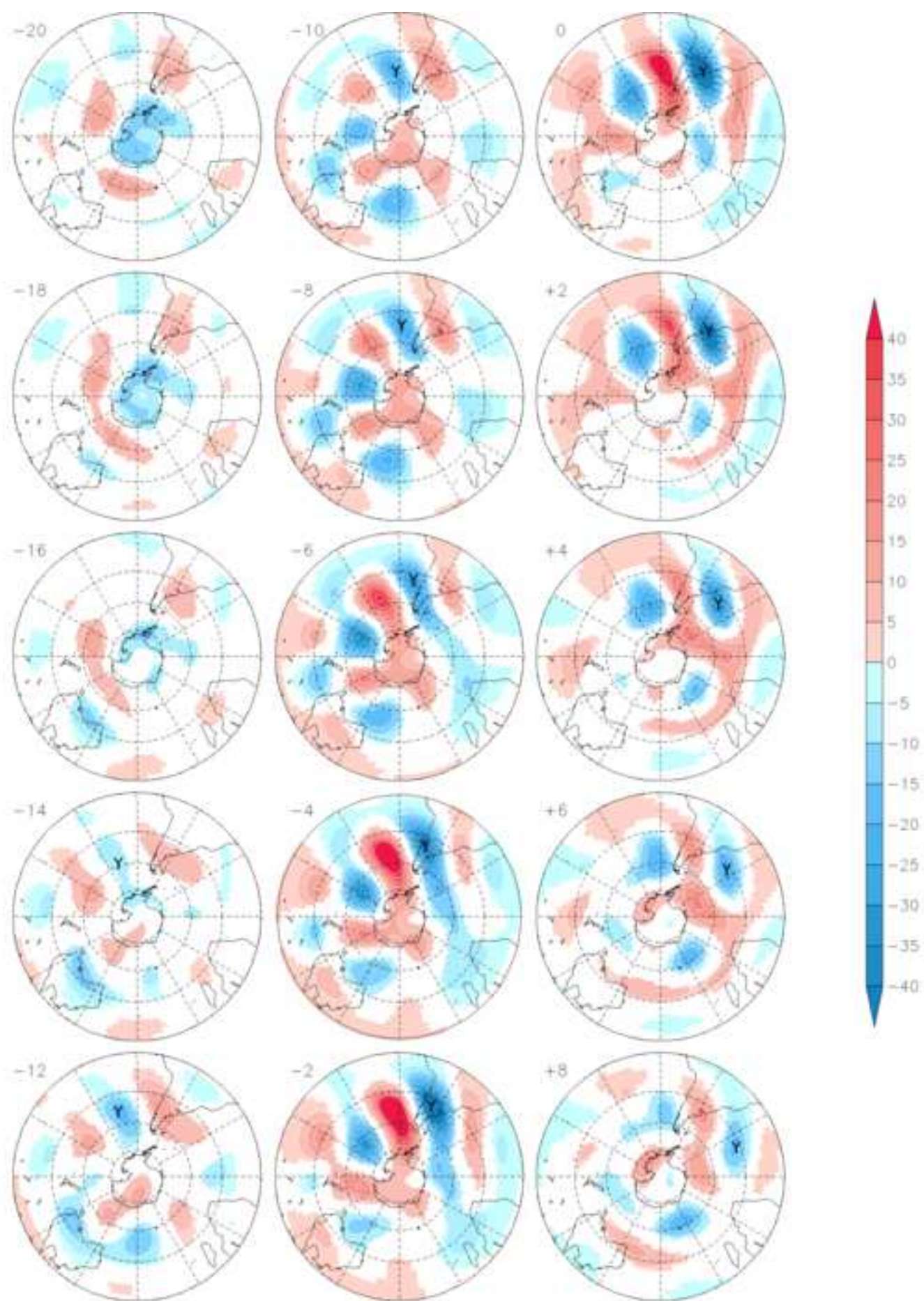


Figure11
[Click here to download high resolution image](#)

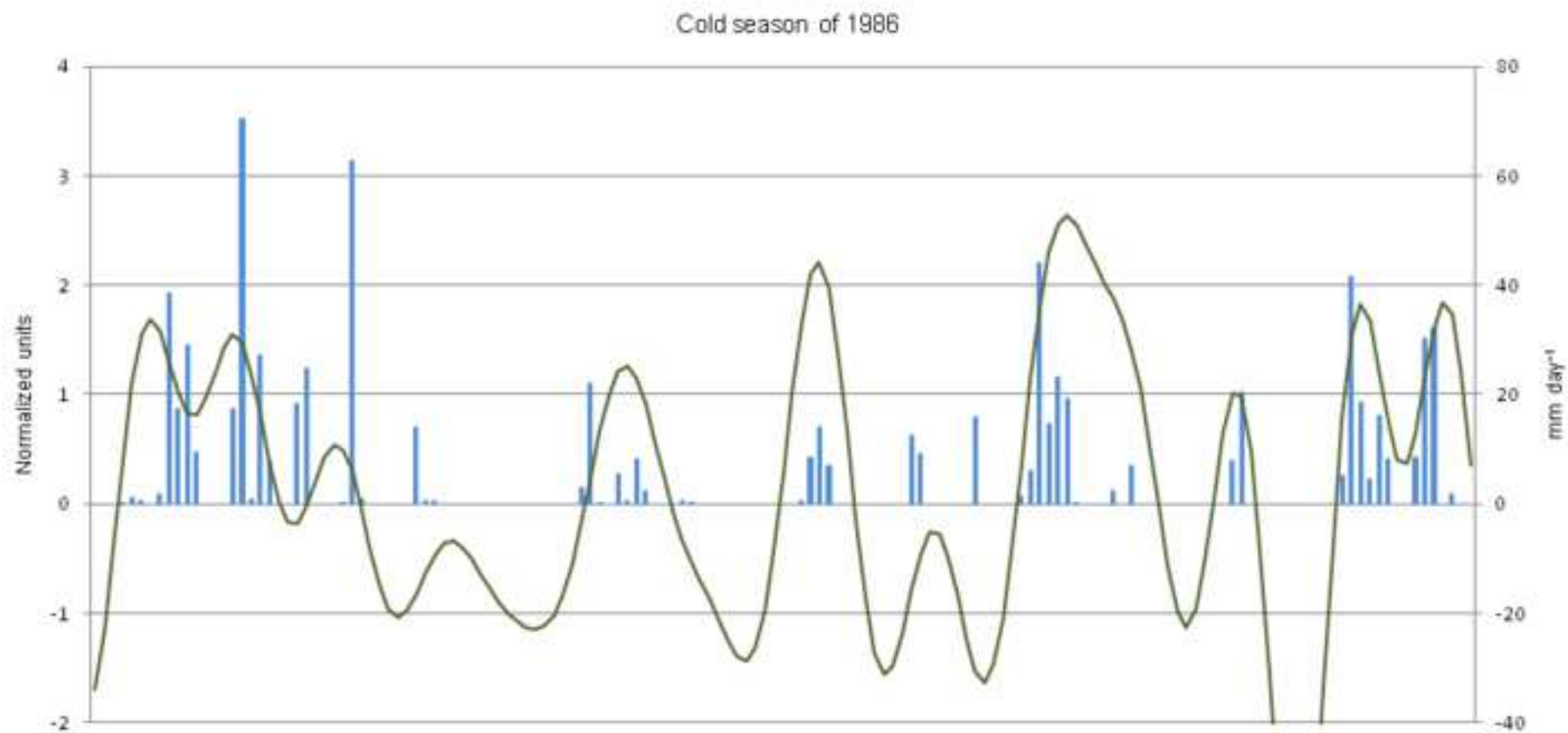


Figure12

[Click here to download high resolution image](#)

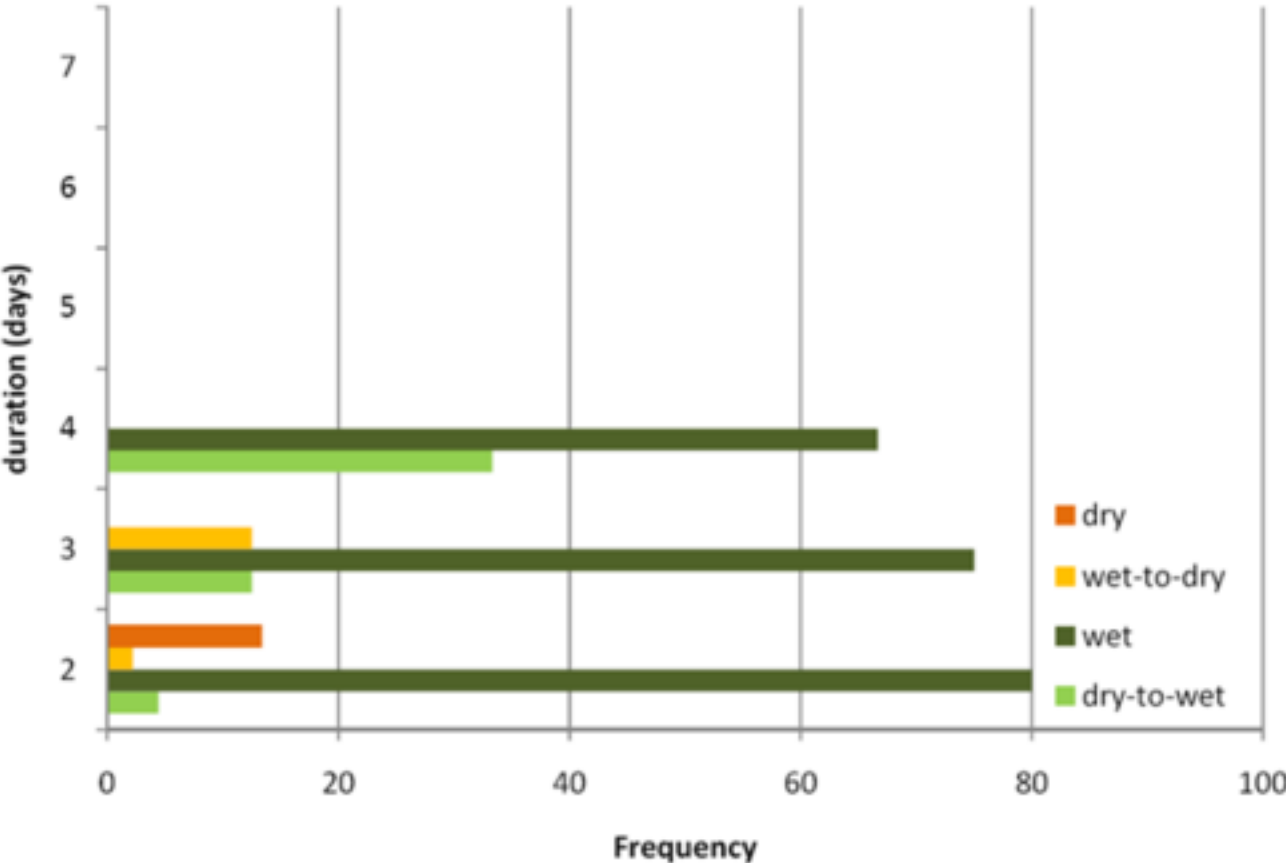
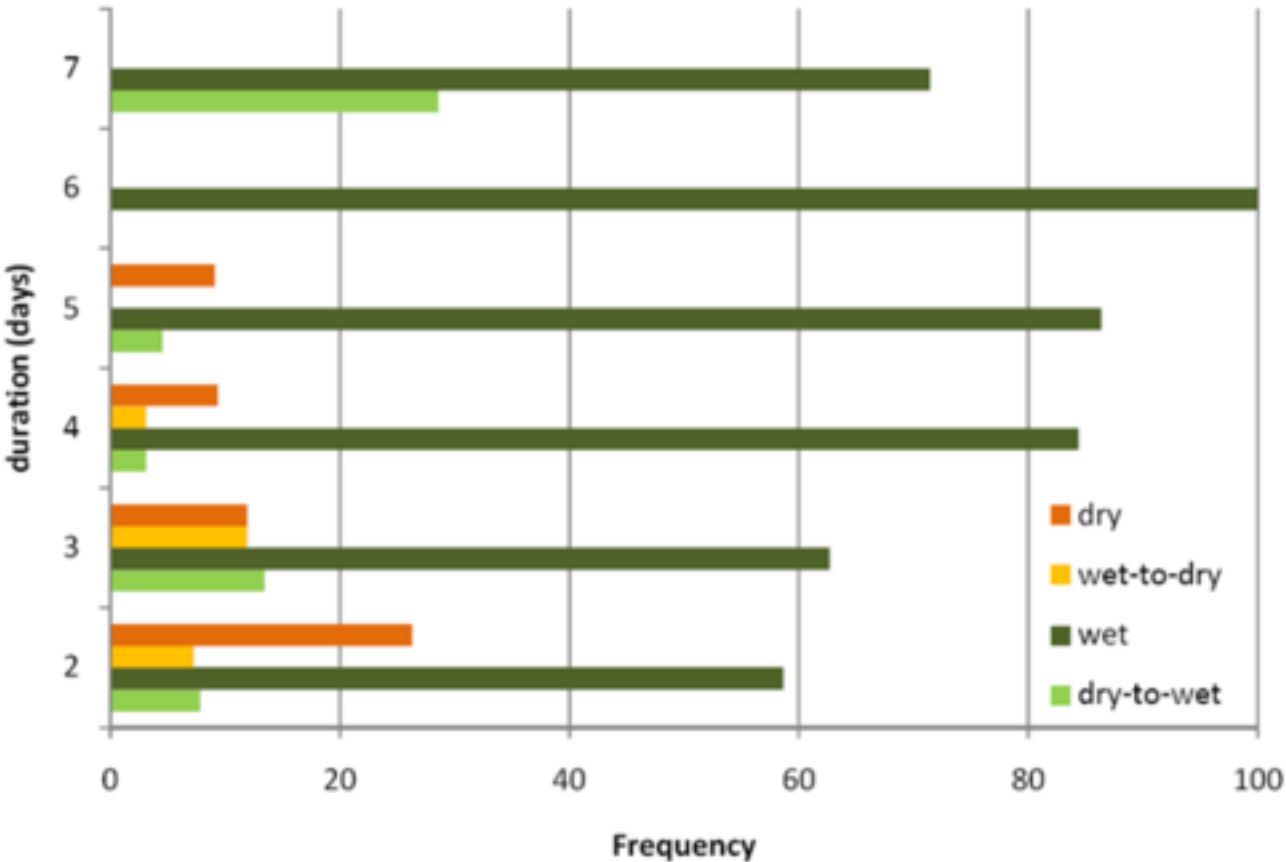


Figure13

[Click here to download high resolution image](#)

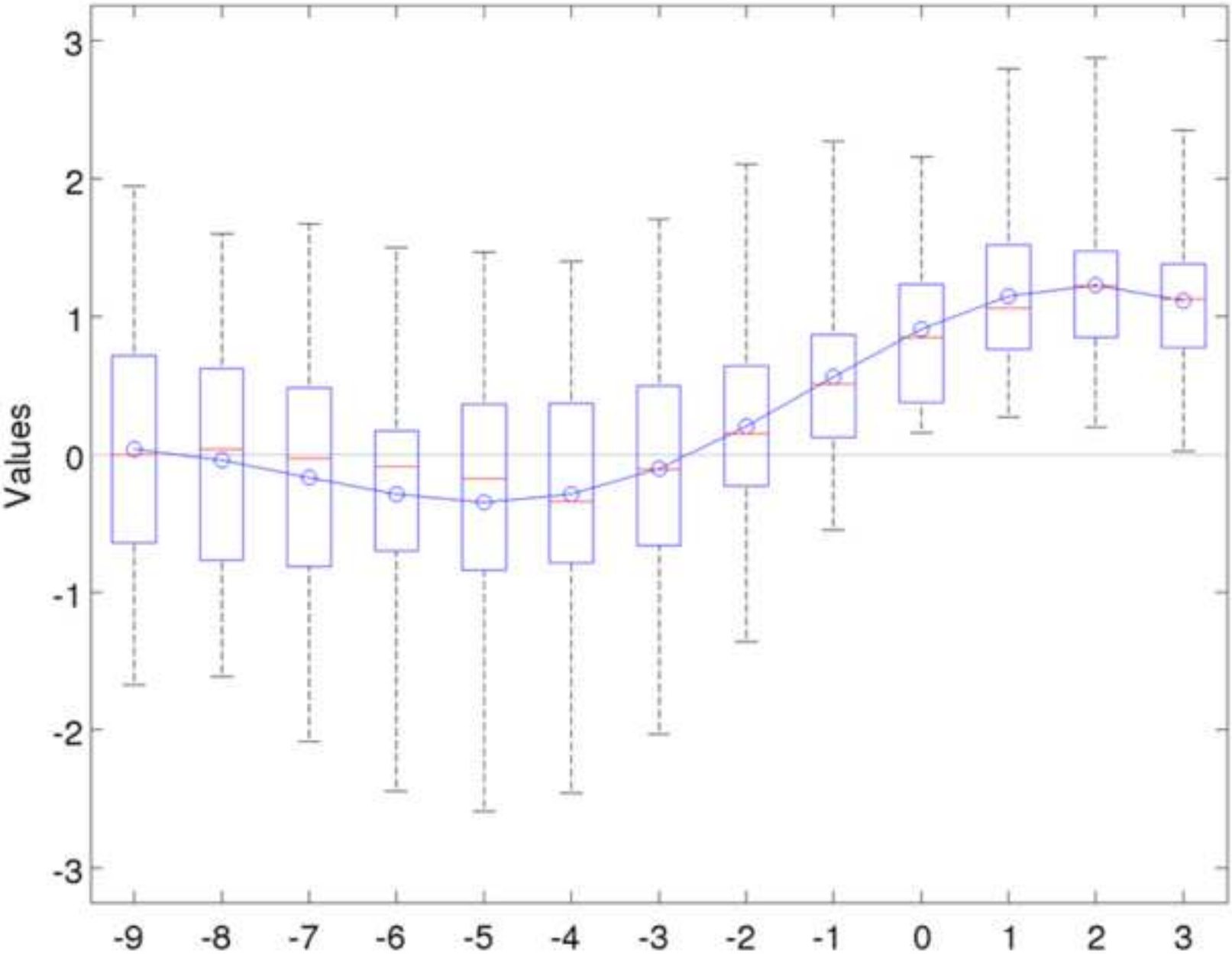


Figure14
[Click here to download high resolution image](#)

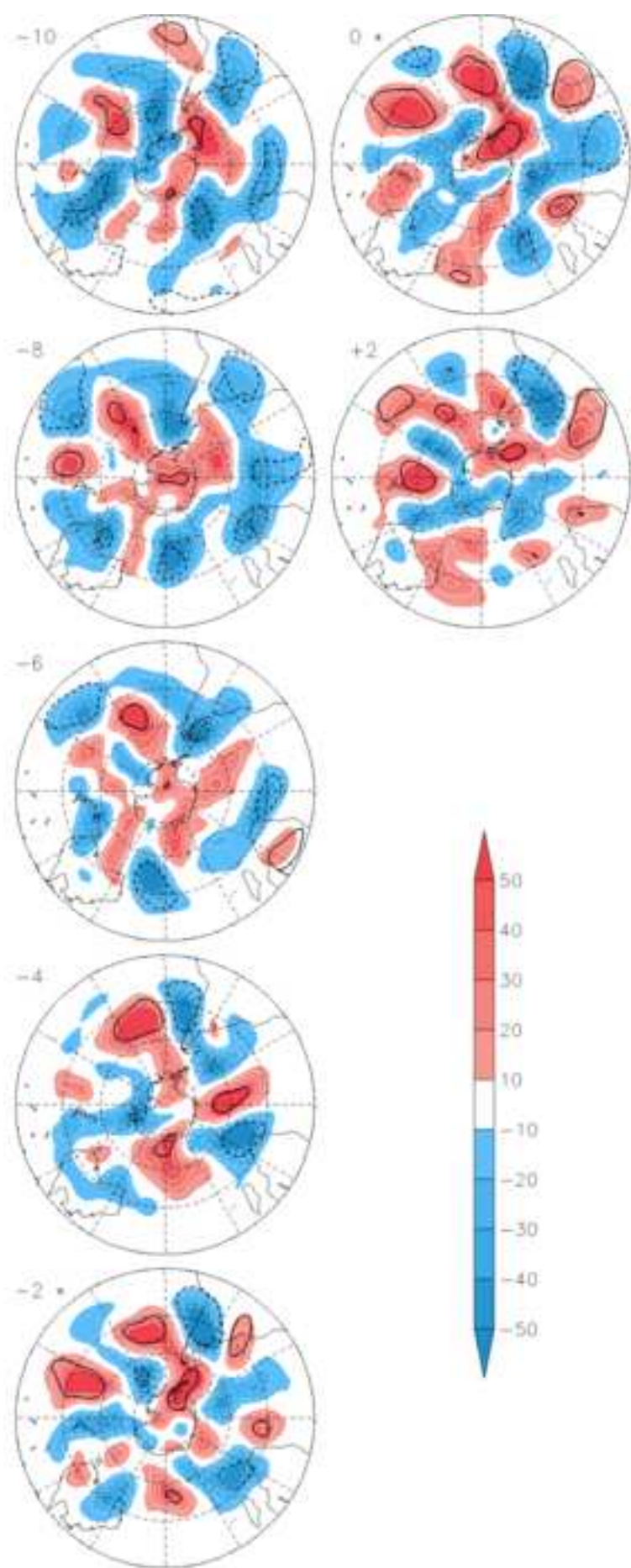


Figure15

[Click here to download high resolution image](#)

